Research Article

SOHAG JOURNAL OF SCIENCES

https://doi.org/10.21608/sjsci.2025.405370.1294

Magnetic Imaging of Subsurface Lineaments for Geotechnical Applications: A Case Study from the Sohag University Campus, Egypt

Abdelabaset M. Abudeif [1]*, Mohammed A. Mohammed [1], Mohsen M. Attia [1], Mohamed M. Khalifa [2], Hossameldeen A. Gaber [1] and Marwa I. Mahmoud [1]

[1]*Geology departement, Faculty of science, Sohag University*
[2]*National Research Institute of Astronomy and Geophysics, Helwan, Egypt*

**Corresponding author's Email:* *a.abudeif @science.sohag.edu.eg*

Received: 18-07-2025, **Revised:** 12/08/2025, **Accepted:** 14/08/2025
Published online: 30/08/2025

Abstract: This study applies the ground magnetic surveying method to investigate shallow subsurface structural lineaments within the Sohag University campus at El-Kawamel for potential engineering purposes. A detailed magnetic survey was conducted over an area of approximately 0.2 square kilometers using a high-sensitivity GEM GSM-19 Overhauser magnetometer. The survey involved six systematically spaced profiles oriented in an east-west direction with 50-meter spacing, employing a zigzag acquisition pattern to ensure full coverage of the site. A total of 1,487 magnetic readings were collected under carefully controlled conditions to minimize noise. Advanced data processing techniques, including regional–residual separation, tilt derivative (TDR), first vertical derivative (FVD), total horizontal derivative of tilt derivative (THDR_TDR), horizontal gradient (HG), and source edge detection (SED), applied to identify structural features and lineaments. Depth estimation methods such as analytic signal, source parameter imaging (SPI), and 3D Euler deconvolution revealed magnetic sources at depths ranging from about 6 to 75 meters with occasional deeper sources reaching ~113 meters in localized zones. The analysis highlighted dominant N-S, E-W and NW-SE structural trends, which are consistent with regional tectonic settings. The results demonstrate the effectiveness of ground magnetic surveying as a valuable tool for preliminary geotechnical investigations prior to construction.
Keywords: Magnetic method, lineaments, Overhauser magnetometer, Sohag University, El-Kawamel.

1. Introduction

In recent years, the use of geophysical methods in civil and environmental engineering has gained increasing importance, particularly for the early detection of subsurface hazards that may affect construction projects [1]. The rising incidence of structural failures has emphasized the necessity of conducting thorough geophysical investigations before initiating any construction activities [2]. Geophysical techniques provide valuable information for identifying potentially hazardous subsurface conditions that may pose risks to engineering structures [3]. According to Soupios et al. [4], these methods are highly effective in detecting subsurface anomalies based on the physical contrasts between different geological layers. Among various geophysical approaches, magnetic methods can be employed in foundation investigations, offering an efficient means to explore shallow subsurface features with high resolution [1]. When integrated with other methods such as Very Low Frequency (VLF) and seismic surveys, magnetic surveys can significantly enhance site characterization and assist engineers in making informed decisions regarding the design and placement of foundation structures.

This study aims to apply the ground magnetic method to investigate shallow subsurface structural lineaments such as fractures, joints and faults that may have engineering significance. The survey was conducted using the Overhauser magnetometer, available at the Geology Department of Sohag University, due to its high sensitivity and efficiency in detecting minor variations in the Earth's magnetic field.

The primary goal is to detect and map subsurface structural features that could influence future construction and development plans. This investigation was carried out at a site located within the Sohag University campus in El-Kawamel, covering an area of approximately 0.2 square kilometers, shaped roughly as a rectangle measuring about 670 meters in length and 300 meters in width (Fig. 1). The study area lies between the latitudes 31°39′36.72″ N to 31°40′0.84″ N and longitudes 26°26′59.28″ E to 26°27′10.08″ E.

2. Geological Setting

Mahran [5] showed that the sedimentary sequence of Sohag area consists of many rock units range from Lower Eocene to Recent (Fig. 2). These formations can be summarized as follows:

2.1. Thebes Formation (Lower Eocene)

This formation consists predominantly of thickly layered to massive limestone, often interbedded with marl deposits. It is well known for containing abundant flint nodules, which formed through diagenetic silica replacement processes. The marls and limestones are rich in marine fossils, especially Nummulites and planktonic foraminifera, indicating that these sediments were deposited in a warm, shallow marine environment with high biological productivity during the Eocene period [6].

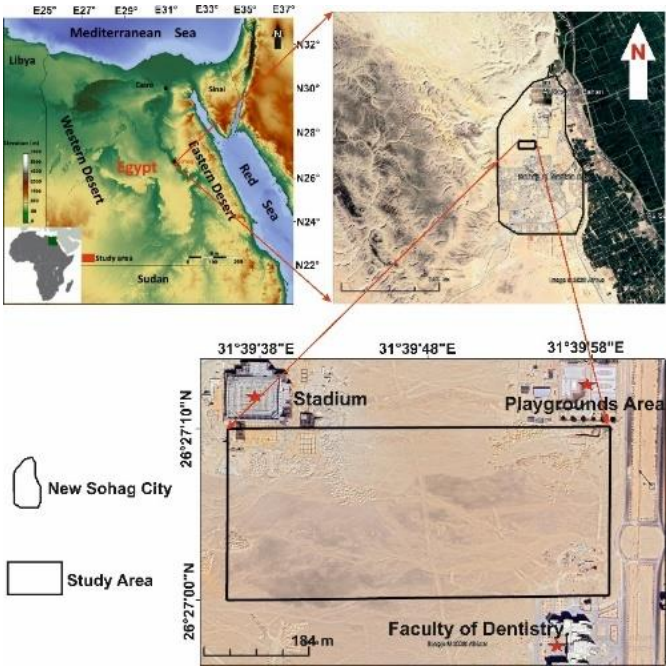

Figure 1: A) General location map of Sohag University Campus, B) Landsat image showing the location of study site and its surroundings. C) Enlargement of the study site.

2.2. Drunka Formation (Lower Eocene)

Composed of medium- to thick-bedded limestone, the Drunka Formation is characterized by the presence of siliceous concretions of various sizes, which likely resulted from post-depositional silica enrichment. This formation also displays significant bioturbation in some layers, where sediment mixing by burrowing organisms reflects active benthic life and oxygenated seabed conditions. These features suggest deposition in a dynamic marine setting with fluctuating chemical and biological conditions [6].

2.3. Katkut Formation (Late oligocene).

The Katkut Formation, exposed west of Sohag, Egypt, consists mainly of coarse clastic sediments, including gravels and sand, deposited unconformably over the Eocene Drunka Formation. It is interpreted to have formed during the Late Oligocene to Early–Late Miocene in fluvial environments dominated by braided and sinuous streams under relatively humid climatic conditions [7].

2.4. Madmoud Formation (Late Miocene/Pliocene).

According to Said [8], this unit is composed of two distinct sections. The upper part comprises brown to yellow siltstones, sandstones, and claystones formed in fluvial environments. The lower part contains interbedded clay, silt, and fine sandstone, indicative of floodplain and deltaic depositional settings. These sediments signify notable fluvial aggradation during the Pliocene reactivation of the river, likely influenced by tectonic uplift or changes in the Nile's base level.

2.5. Issawia Formation (Late Pliocene / Early Pleistocene)

The Issawia Formation consists of clastic sediments deposited along the margins of ancient lakes, with carbonate facies occurring in the central parts of these basins. This dual nature reflects changes in lake levels, with coarse sediments deposited near the shores and finer, carbonate-rich sediments accumulating in the deeper, quieter central lake zones. The formation represents a mixed fluvial-lacustrine environment shaped by climatic oscillations during the Pliocene-Pleistocene transition [9].

2.6. Armant Formation (Early Pleistocene).

This formation consists of alternating layers of fine-grained clastics and carbonate-rich travertine, indicating intervals of clastic fluvial deposition interrupted by episodes of spring-fed carbonate precipitation. Such characteristics suggest episodic sedimentation within a tectonically controlled valley, influenced by localized spring activity [8].

2.7. Qena Formation (Middle Pleistocene)

This formation is made up of quartz-rich sands and gravels, with a notable absence of igneous and metamorphic rock fragments. Its composition suggests that the sediments were derived from mature, well-weathered sources and transported over long distances by river systems before deposition. The Qena Formation is interpreted as a fluvial deposit formed under conditions dominated by mechanical weathering and sediment sorting [9].

2.8. Dandara Formation (Late Pleistocene)

The Dandara Formation is characterized by fine-grained fluvial sediments, consisting predominantly of sand and silt layers that were deposited under low-energy conditions. These sediments accumulated in floodplain environments or overbank settings, where river currents lost their strength and allowed fine materials to settle. This formation reflects periods of relative river stability with limited sediment transport capacity [10].

2.9. Cultivated Lands (Neogene and Quaternary – Recent/Holocene)

These deposits cover extensive areas of the Nile floodplain and are composed primarily of clay and silt, interlayered with occasional sandstone beds. They represent recent and historical flood events, during which the Nile deposited fine sediments across its floodplain. These deposits are typical of modern overbank flooding and are associated with fertile agricultural lands [4].

Structurally, the Sohag Basin occupies an active segment of the Nile Valley shaped by successive tectonic regimes from the Cretaceous to the Quaternary. The basin records a transition from full- to half-graben geometries, as documented by Tawfik and Hassan [11], indicating syn-depositional extensional tectonics during the Late Miocene–Early Quaternary. Mahran [5] attributes these features to differential subsidence and accommodation space generation resulting from basin-margin fault reactivation. These structural controls strongly influenced sediment dispersal patterns, the preservation of paleosol horizons, and the architecture of the Plio–Pleistocene stratigraphy. The surrounding Eocene plateau is dissected by normal and strike-slip faults, as well as folds, which are largely related to tensional rather than compressional stresses [12]. Youssef [13] reported that the main fault orientations correspond to the NW–SE Gulf of Suez trend, the NE–SW Aqaba trend, and the E–W transverse trend, reflecting the interplay of regional tectonic systems.

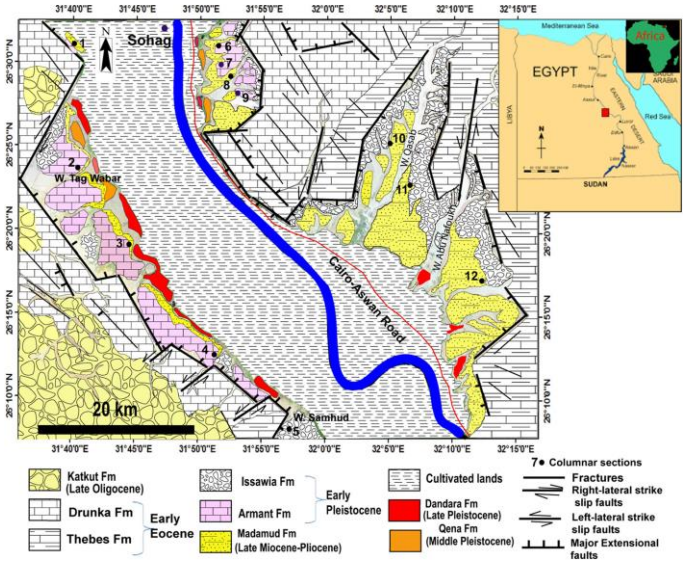

Figure 2: Simplified geological map of the Sohag basin [5].

3. Materials and Methods

3.1. Regional and Residual seperation

Spectral analysis, which is theoretically based on the fast Fourier transform (FFT), is a common technique used to separate regional and residual components from aeromagnetic data. This method has been described by several researchers [14-16]. Through this process, a two-dimensional radially averaged power spectrum was generated (Fig. 6). The cutoff wavenumber, set at 10 cycles/km, was determined by identifying the point where the slope of the spectrum changes.

3.2. Edge detection methods

3.2.1. Tilt derivative (TDR) and total horizontal derivative of tilt derivative (THDR_TDR).

The tilt angle derivative (TDR) filter was initially introduced by Miller and Singh, [17] and later developed by Verduzco et al., [18]. It is commonly used to map potential mineralization zones and subsurface basement structures [19]. This method does not require prior knowledge of the source's structural index, yet it can effectively estimate both the horizontal position and depth of magnetic sources. Salem et al., [20,21] demonstrated that the tilt angle values range between $\pm\pi/2$. TDR has gained significant attention due to its straightforward application and practical effectiveness [22]. It can be expressed by Equation (1) as follows:

$$\mathbf{TDR\ or\ \theta = \tan^{-1}\left(\frac{FVD}{THDR}\right)} \quad \text{(1)}$$

where θ is the local phase, FVD is the first vertical derivative and THDR is the total horizontal derivative.

The tilt derivatives exhibit notable changes with varying inclinations; however, at inclinations of 0° and 90°, the zero-contour line closely follows the edges of the model structures. Positive values are observed directly above the sources, while negative values appear farther from them [22].

Verduzco et al. [18] introduced an edge detection method called the Total Horizontal Derivative of the Tilt Derivative (THDR_TDR). It is defined as the square root of the sum of the squares of the derivatives of the TDR in the x and y directions, as expressed in Equation (2):

$$\mathbf{THDR\_TDR} = \sqrt{\left(\frac{\partial TDR}{\partial x}\right)^2 + \left(\frac{\partial TDR}{\partial y}\right)^2} \quad \text{(2)}$$

3.2.2 First vertical derivative (FVD) method

The first vertical derivative (FVD) of the magnetic field reflects the rate of change of field intensity with respect to elevation. As shown in Equation (3), calculating the FVD effectively attenuates long-wavelength (regional) components of the magnetic field, while amplifying signals from shallow sources. This enhances the resolution of closely spaced anomalies, allowing for better differentiation between nearby geological structures [23].

$$\boldsymbol{FVD = \frac{\partial f}{\partial z}} \quad \text{(3)}$$

3.2.3. Horizontal gradient (H-gradient) method

The horizontal gradient technique was initially introduced by Roest et al. [24] and has been widely applied in the interpretation of RTP data. This method is regarded as one of the simplest approaches for identifying contact locations [25,26]. The H-gradient technique is often considered the most straightforward method for estimating the positions of subsurface contacts, primarily due to its low sensitivity to noise, as it only requires the calculation of the first horizontal derivatives of the magnetic field [27]. The horizontal gradient magnitude (HGM) can be calculated using Equation (4):

$$\mathbf{HGM} = \sqrt{\left(\frac{\partial M}{\partial x}\right)^2 + \left(\frac{\partial M}{\partial y}\right)^2} \quad \text{...(4)}$$

M is the magnetic field.

3.2.4. Source edge detection (SED) method

The Source Edge Detection (SED) method is designed to enhance the edges of geological sources by identifying points where the data exhibit maximum gradients, which generally correspond to anomaly boundaries. By analyzing local gradients, the SED technique can detect peaks and edges (geological contacts) in magnetic data [28]. It identifies abrupt horizontal changes in rock densities or crustal magnetizations by locating maxima on grids derived from the horizontal gradient, tilt derivative (TDR), and horizontal derivative of TDR (THDR_TDR) [29]. While often used alongside the horizontal gradient method, SED is specifically optimized to precisely locate edges rather than simply highlighting high-gradient zones.

3.3. Estimation the depth to the basement complex

3.3.1. Analytic signal depth technique

This method, also known as the total gradient technique, is highly effective for delineating the edges of magnetic source bodies and is widely applied using Geosoft Oasis Montaj software, version 8.4 [14]. According to Roest et al., [24] and Nabighian [30], the analytic signal technique assumes that the sources are isolated, dipping contacts separating thick geological units. The analytic signal magnitude is calculated as the square root of the sum of the squares of the magnetic field's vertical and horizontal derivatives [31], as expressed in Equation (5):

$$\boldsymbol{AS} = \sqrt{\left(\frac{\partial f}{\partial x}\right)^2 + \left(\frac{\partial f}{\partial y}\right)^2 + \left(\frac{\partial f}{\partial z}\right)^2} \quad \text{...(5)}$$

One of the key advantages of using the analytic signal (AS) method is its independence from the magnetic field's inclination when identifying magnetic parameters from anomalies. With

minimal assumptions about the source body, typically considered a two-dimensional magnetic structure, the AS method effectively locates and estimates the depth of magnetic sources, such as steps, contacts, horizontal cylinders, or dikes. In these geological models, the amplitude of the AS displays a symmetric, bell-shaped curve centered directly over the source body.

The analytic signal of the first vertical derivative (AS1) can be derived from Equation (6).

$$\mathbf{AS1} = \sqrt{\left(\frac{\partial \mathbf{FVD}}{\partial \mathbf{x}}\right)^2 + \left(\frac{\partial \mathbf{FVD}}{\partial \mathbf{y}}\right)^2 + \left(\frac{\partial \mathbf{FVD}}{\partial \mathbf{z}}\right)^2} \quad \text{.....(6)}$$

where: the FVD is the first vertical derivative of the RTP.

So, to calculate the depth to magnetic source Equation (7) is used:

$$\mathbf{D} = \frac{\mathbf{AS}}{\mathbf{As1}} * \mathbf{N} \text{.....(7)}$$

Here, D represents the depth of the magnetic sources, and N refers to the structural index, which reflects the geometry of the magnetic source. For instance, $N = 1$ corresponds to a magnetic contact, $N = 2$ represents a thin dike, $N = 3$ indicates a pipe-like body, and $N = 4$ corresponds to a spherical source [32].

3.3.2. Source parameter imaging (SPI) technique

The Source Parameter Imaging (SPI) technique, also referred to as the local wavenumber method, is used to estimate the depth of magnetic sources by extending the concept of the analytic signal [33]. In this method, the local wavenumber function is expressed by Equation (8):

$$\mathbf{k} = \frac{\frac{\partial^2 \mathbf{f}}{\partial \mathbf{x} \partial \mathbf{z}} \frac{\partial \mathbf{f}}{\partial \mathbf{x}} - \frac{\partial^2 \mathbf{f}}{\partial \mathbf{x}^2} \frac{\partial \mathbf{f}}{\partial \mathbf{z}}}{\left(\frac{\partial \mathbf{f}}{\partial \mathbf{x}}\right)^2 + \left(\frac{\partial \mathbf{f}}{\partial \mathbf{z}}\right)^2} \quad \text{.....(8)}$$

Regardless of the magnetic inclination, declination, dip, strike, or any residual magnetization, the maxima of the local wavenumber (k) for a dipping contact are located directly above the isolated edges of the contact [33]. The depth to the source edge can be estimated using Equation (9), which is derived from the reciprocal of the local wavenumber:

$$\mathbf{Depth}_{(\mathbf{x=0})} = \frac{\mathbf{1}}{\mathbf{k_{max}}} \quad \text{.....(9)}$$

Where: k_{max} is the maximum value of the local number k over the step source.

Depths can be estimated without requiring any assumptions about the thickness of the source bodies, as the local wavenumber exhibits maxima directly above isolated contacts [34]. The SPI method was compared to the analytic signal technique by Phillips [27], highlighting differences between the two approaches in terms of underlying assumptions, accuracy, sensitivity to noise, and the way they handle overlapping anomalies.

3.3.3. Euler deconvolution (ED) technique

Thompson [35] introduced this technique for estimating depths and identifying multiple sources within a specific area. The 3D Euler deconvolution equation, as defined by Thompson [35] and Reid et al. [32], is expressed as:

$$\frac{\partial f}{\partial x}(x - x_0) + \frac{\partial f}{\partial y}(y - y_0) + \frac{\partial f}{\partial z}(Z - Z_0) = SI(B - f) \text{..... (10)}$$

Where f represents the observed field at the location (x_0, y_0, z_0), B denotes the background or regional field value at point (x, y, z), and SI refers to the structural index, also known as the degree of homogeneity.

The structural index (N) characterizes the homogeneity of the field and is directly associated with specific source geometries [36]. Accurate selection of N is essential for reliable depth estimation and should be based on geological understanding of the area [36, 37]. Several computational techniques have been developed to assist in determining the appropriate structural index, including methods proposed by Barbosa et al. [35], Salem and Ravat [39] and Melo and Barbosa [40]. Table 1 summarizes typical structural index values for common, idealized geological structures.

3.4. Subsurface trends

The Center for Exploration Targeting (CET) grid analysis method was applied to extract and evaluate structural lineaments from the RTP magnetic data within the study area. These structural features were then statistically analyzed and presented as rose diagrams using Rockware version 16 software [41]. The azimuths and lengths of the detected lineaments were measured and analyzed to calculate their length and number percentages (L% and N%), along with their length-to-number (L/N) ratios.

By tracing and statistically analyzing the magnetic lineaments, considering their number (N), total length (L), L/N ratios, and orientations, the major tectonic trends influencing the study area were identified.

Table 1: The structural indices of some simple-shaped sources in potential field studies [37]. In this study, SI = 0 and SI = 1 were applied to Euler Deconvolution solutions: SI = 0 targeted simple geological contacts, and SI = 1 targeted vertical or steeply dipping structures (e.g., faults, fractures, dykes).

Source	No. of Infinite Dimensions	Magnetic	Depth Relative to…
Sphere	0	3	Center
Vertical line / pipe / cylinder	1	2	Top
Horizontal line / cylinder	1	2	Center
Dyke	2	1	Top
Sill	2	1	Center
Contact	3	0	Top

The results of this statistical trend analysis (L%, N%, and L/N ratios) provide insights into the distribution of fractures, revealing the cumulative lengths and frequencies of specific lineament sets across different parts of the study area, and clearly indicating the dominant structural orientations [42].

4. Survey layout

A comprehensive land magnetic survey was conducted over an area of approximately 0.2 square kilometers. The survey employed a GEM GSM-19 Overhauser magnetometer, provided by the Geology Department at Sohag University. This instrument offers high sensitivity (0.022 nT) and fine resolution (0.01 nT), making it highly effective for detecting subtle variations in the Earth's magnetic field. During the survey, the sensor was mounted at a height of 1.8 meters above the ground surface (Fig. 3). The device is portable and operates independently of location, temperature, or sensor orientation. Moreover, it is equipped with an integrated Global Positioning System (GPS), which automatically records the coordinates of each measurement point.

Prior to data collection, all metallic objects present on the ground surface were carefully removed to minimize potential noise and ensure the accuracy of the measurements. The survey was performed under optimal, noise-free conditions.

Data acquisition was conducted along six profiles strategically distributed to cover the entire study area (Fig. 4). A total of 1487 magnetic readings were collected. The magnetometer was configured for continuous data acquisition, recording measurements at two-second intervals. The profiles were spaced nearly 50 meters apart, and the survey lines were oriented in an East-West direction and employed in a zigzag pattern to enhance data coverage and maintain consistency in measurements across the area.

5. Data interpretation and discussion

5.1. Total magnetic intensity (TMI) map

The Total Magnetic Intensity (TMI) map illustrates the combined influence of the regional geomagnetic field and local magnetic anomalies caused by subsurface variations in magnetic susceptibility. This map (Fig. 5) clearly highlights zones of both high and low magnetic intensity. High magnetic intensity zones are depicted by warm colors, including violet, red, and yellow, with values ranging from 42,332 nT to 42,366.5 nT. In contrast, low magnetic intensity zones are represented by cool colors such as blue and green, with values ranging from 42,315 nT to 42,332 nT.

Figure 3: Field photograph of data acquision using GEM GSM-19 Overhauser magnetometer. The operator was free of any steel or objects that may affect magnetic data.

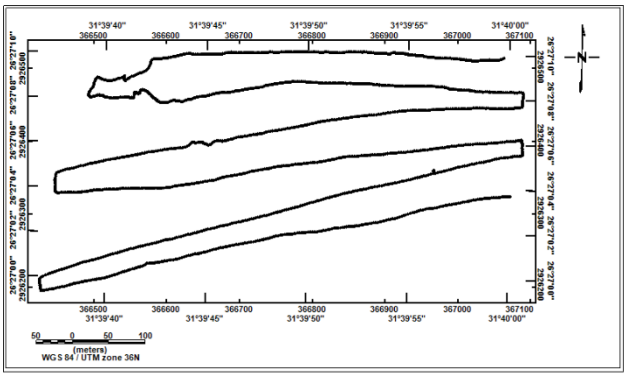

Figure 4: Layout of survey lines taken in nearly E-W direction with nearly 50 meters profile spacing.

The high magnetic anomalies are primarily concentrated in three main regions within the study area: the northwestern, northeastern, and southeastern parts of the map. On the other hand, low magnetic anomalies are mostly observed in the northern section of the area, trending in an east-west direction. The magnetic anomalies exhibit a variety of shapes, including rounded, sub-rounded, and elongated forms, reflecting the complexity of the subsurface geological features.

5.2. Reduce to the magnetic pole (RTP) map

The Reduction to the Magnetic Pole (RTP) is one of the key transformation techniques applied to magnetic data to facilitate its interpretation. This process effectively minimizes the influence of the Earth's magnetic field direction, making the interpretation of magnetic anomalies more straightforward and independent of the magnetization direction of the sources. As a result, RTP shifts magnetic anomalies to their correct locations directly above their causative bodies, thereby enhancing the accuracy and reliability of the interpretation [41].

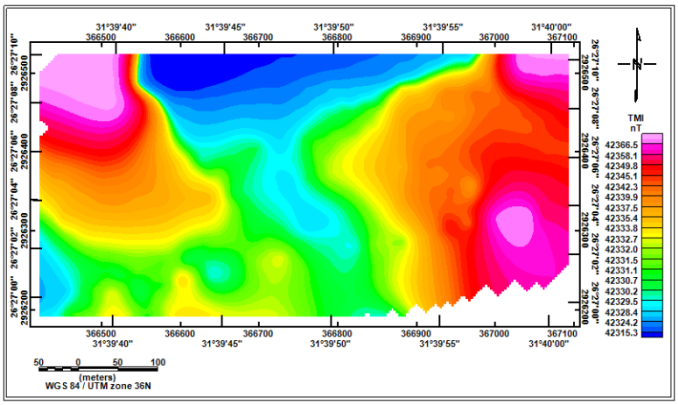

Figure 5: Total magnetic intensity (TMI) map of the studied area.

By applying RTP, the asymmetrical anomalies caused by the Earth's magnetic field inclination and declination are corrected, aligning the anomalies properly towards the north and allowing for more precise geological analysis.

The RTP map (Fig. 6) was generated from the Total Magnetic Intensity (TMI) map using Geosoft Oasis Montaj software, version 8.4 [14]. The International Geomagnetic Reference Field (IGRF) parameters used in this process included a magnetic field strength of 42,300 nT, an inclination of 39.03°N, and a declination of 4.4°E.

Examination of the RTP map reveals two prominent high (positive) magnetic anomalies located in the eastern and western portions of the study area. Additionally, a distinct low (negative) anomaly appears in the central part of the map. These magnetic anomalies generally trend in a nearly north-south direction.

Detailed analysis of the shapes and distribution of these anomalies suggests the presence of a local fault zone that separates the positive and negative anomalies, particularly noticeable in the eastern section of the study area. This structural feature likely plays a significant role in controlling the distribution of the subsurface magnetic sources.

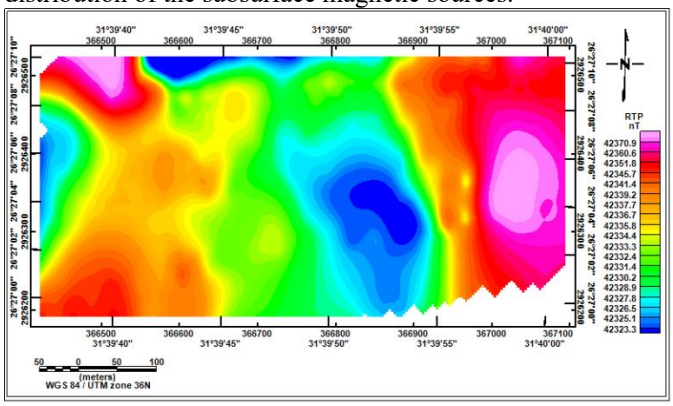

Figure 6: Reduce to magnetic pole (RTP) map of the studied area.

5.3. Regional–residual separation

The RTP data was further processed using the Fast Fourier Transform (FFT) technique to compute the energy spectrum and generate the two-dimensional (2D) power spectrum. This spectral analysis helps in estimating the average depths of magnetic sources. By analyzing the variation in the slope of the power spectrum curve, the curve is divided into distinct linear segments, each representing magnetic sources at different depths. The slope of each segment corresponds to the depth of the associated magnetic sources.

The average depth of each magnetic source contributing to the respective segment of the spectrum can be determined using Equation (11).

$$\textbf{Depth} = \frac{-\textbf{slope}}{4\pi} \quad \text{.....(11)}$$

The power spectrum curve (Fig. 7) primarily consists of two distinct linear segments. The first segment, shown in red, spans the low wavenumber range from 0 km^{-1} to 10 km^{-1}. The slope of this segment indicates the average depth to the deeper magnetic sources, which is calculated to be approximately 60 meters. The second segment, displayed in blue, also lies within the low wavenumber range, extending from 10 km^{-1} to 20 km^{-1}. The slope of this segment corresponds to the average depth of the shallower magnetic sources, estimated at around 20 meters.

Wavenumbers higher than 20 km^{-1} are generally associated with noise or insignificant geological information and are therefore not considered in the depth estimation process. This spectral analysis effectively distinguishes between shallow and deep magnetic sources within the study area. Here cutoff wave number 10 cycles/km was used to get the residual and regional magnetic anomaly maps.

A comparison between the regional map and the RTP map reveals that similar anomalies appear in both; however, in the regional map, these anomalies are presented in a smoother, more generalized manner due to the filtering of shallow effects. The same general trends of anomalies, ranging from north-south (N-S) to north-northwest to south-southeast (NNW-SSE) directions, are clearly visible. The anomalies exhibiting ellipsoidal to elongated shapes.

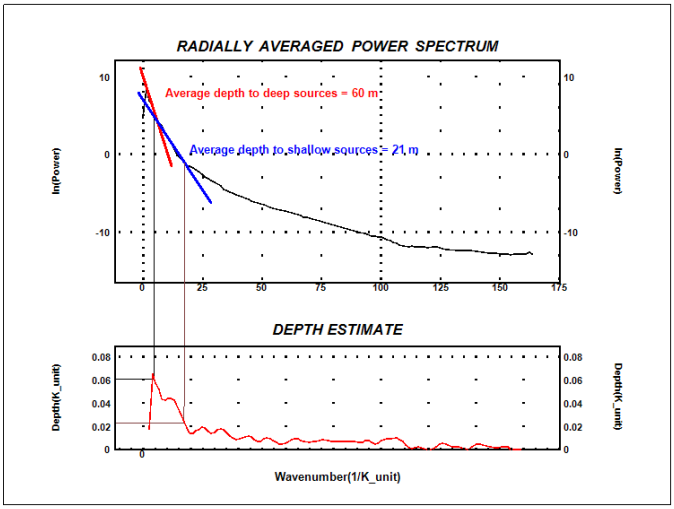

Figure 7: The radially average power spectrum (RAPS) of the study

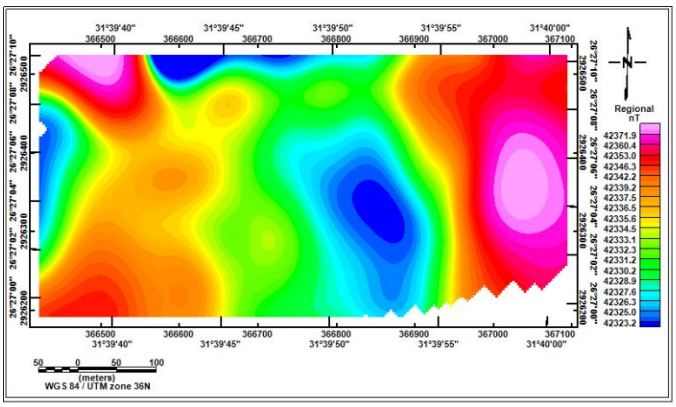

Figure 8: Low-pass (Regional) magnetic map of the studied area.

The high-pass filtered magnetic map (Fig. 9) emphasizes the effects of shallow magnetic sources by removing long-wavelength components related to deeper structures. The map displays magnetic anomalies with values ranging from -4.0 nT to +2.2 nT.

Positive and negative anomalies are alternately distributed across the study area, reflecting variations in near-surface magnetic properties. The anomalies exhibit distinct trends in north-south (N-S), east-west (E-W), and northwest-southeast (NW-SE) directions, which closely align with the orientation of local structural features within the region.

In terms of shape, the anomalies appear as small semi-circular, oval, and elongated forms, indicating shallow subsurface bodies or structural features such as minor faults, fractures, or lithological contacts. These patterns offer valuable insights into the shallow geological framework of the area.

5.4. Edge detection methods

According to Miller and Singh [17], geological structures such as faults, which often appear as magnetic lineaments, can be effectively identified through Tilt Derivative (TDR) analysis. The TDR map (Fig. 10) displays values ranging from -1.42 to +1.14 radians. The black line shown in the map represents the zero-contour line, which marks the boundary between magnetic sources. This contour generally corresponds to zones of sharp changes in magnetic susceptibility, indicating contact zones between contrasting geological units, especially at areas of steep magnetic gradients.

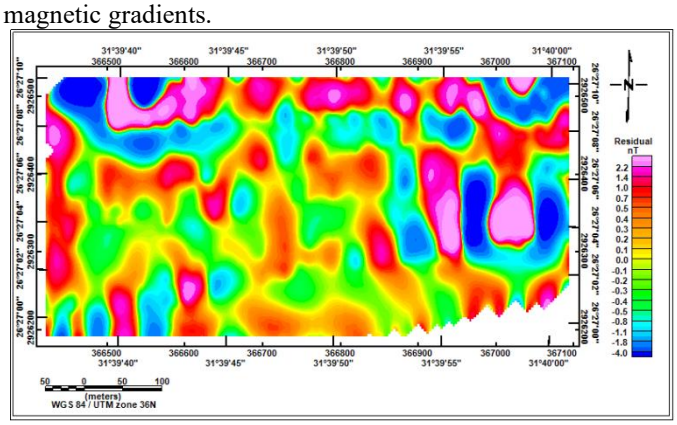

Figure 9: High pass (residual) magnetic map of the studied area.

The TDR map clearly highlights structural trends within the study area, with anomalies oriented in north-south (N-S), east-west (E-W), northwest-southeast (NW-SE), and northeast-southwest (NE-SW) directions, aligning with known structural trends of the region.

As demonstrated by Rajaram [44], the Total Horizontal Derivative of Tilt Derivative (THDR_TDR) method enhances the amplitude of TDR anomalies, allowing for precise delineation of structural boundaries. In this method, the reciprocal of the amplitude of the THDR_TDR anomaly provides an estimate of the depth to the top of the magnetic source.

Furthermore, according to Salem et al. [21], the half-distance between the ±45° radians (±π/4) contours in the TDR map can also be used to estimate the depth to vertically oriented magnetic sources. The THDR_TDR map (Fig. 11) shows the results of this analysis. From the inspection of this map, it is deduced that the depths to magnetic sources within the study area range from approximately 6 meters to 113 meters.

The First Vertical Derivative (FVD) filter was also applied to the RTP data to produce the FVD map (Fig. 12). This map highlights sharp changes in the magnetic field by enhancing shallow, near-surface anomalies and suppressing deeper, regional effects.

The FVD map displays alternating positive and negative anomalies, which closely correspond with the features observed in the TDR map (Fig. 9), both in terms of their direction and structural trends. The anomalies in the FVD map are aligned along the same dominant orientations, reflecting the underlying geological structures.

Similar to the TDR map, the zero-contour line in the FVD map marks the boundary between positive and negative anomalies. This line effectively delineates zones of abrupt changes in magnetic susceptibility, identifying contacts between different geological units or fault zones with high precision.

The horizontal gradient (HG) map of the magnetic data illustrates (Fig. 13) the rate of change in the magnetic field strength along the horizontal plane. This filter is particularly effective in emphasizing edges and boundaries of magnetic sources, as it enhances zones with strong lateral contrasts in magnetic susceptibility. The map clearly reveals the dominant tectonic trends, with the most prominent features oriented in an east-west (E-W) direction. These trends likely correspond to major structural elements such as faults, fractures, or lithological contacts within the study area.

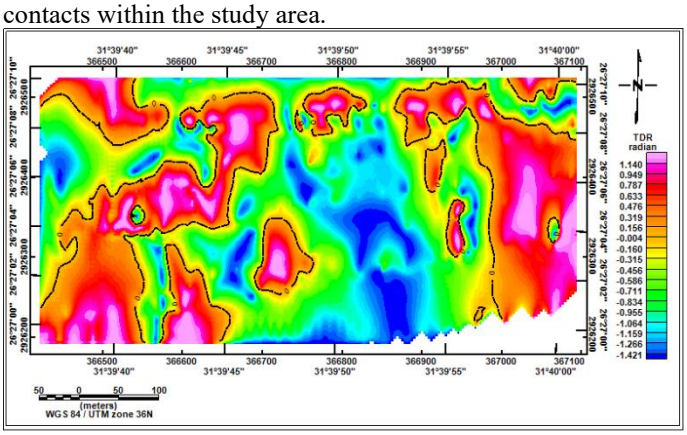

Figure 10: Tilt angle derivative (TDR) map of the studied area.

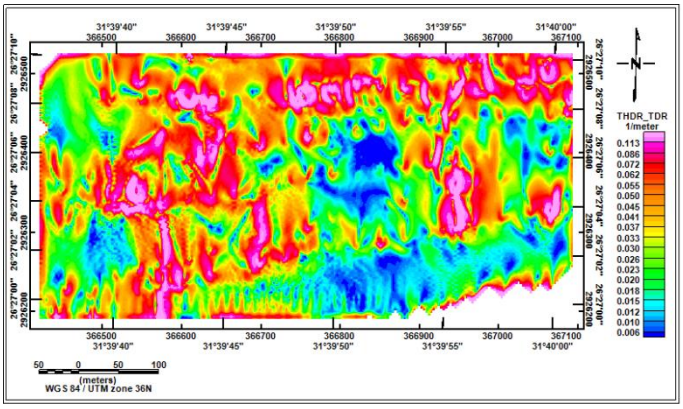

Figure 11: Total horizontal derivatives of the tilt angle derivative (THDR_TDR) map of the studied area.

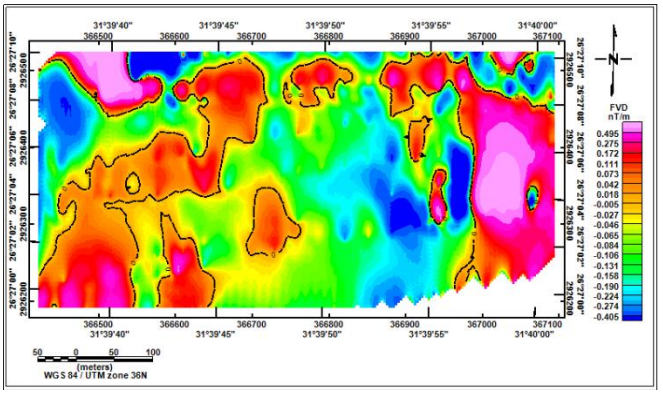

Figure 12: First vertical derivative (FVD) map of the studied area.

5.5. Depth estimation methods

5.5.1 The analytic signal depth map

The analytical signal (AS) approach was applied in the study area to estimate the depth to the basement surface. This method involves several processing steps to accurately define the edges of magnetic sources and calculate their depths.

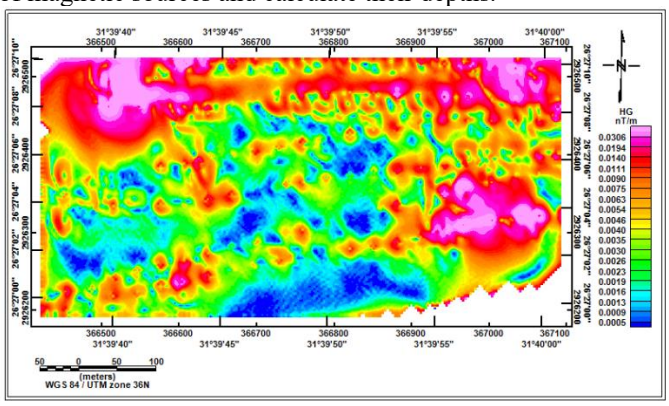

Figure 13: Horizontal gradient (HG) map of the studied area.

5.4.4. The source edge detection (SED) map

The Source Edge Detection (SED) solutions map (Fig. 14) is employed to identify and delineate the edges of magnetic sources. These edges may represent significant geological structures, such as faults, intrusive bodies, or contacts between rocks with contrasting magnetic properties. The detected source boundaries are presented in vector format, allowing for precise interpretation of their strike and potential dip directions [45]. The SED solutions are symbolized in a way that aligns with the outlines of the magnetic anomalies. Moreover, the orientation of these vectors coincides with the direction of the magnetic gradients, further enhancing the accuracy of structural interpretation.

This correspondence between the SED solutions and the magnetic anomalies simplifies the interpretation process and aids in analyzing the shape, extent, and distribution of the magnetic sources across the study area, providing valuable information for geological and structural mapping.

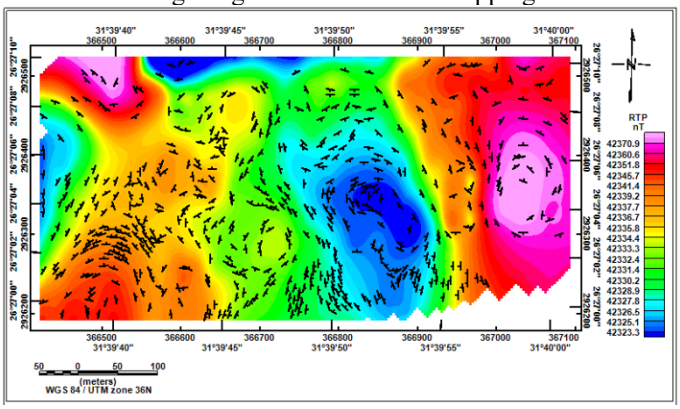

Figure 14: Source edge detection (SED) solutions plotted on the RTP map of the studied area.

First, the analytical signal filter was applied to the RTP map, resulting in the AS map (Fig. 15), which highlights the edges of magnetic sources in both horizontal and vertical directions. This map effectively delineates the locations of subsurface magnetic contrasts.

Next, the same analytical signal filter was applied to the FVD map, producing the analytical signal of the first vertical derivative (AS1) map (Fig. 16). This map further enhances near-surface anomalies and provides additional detail regarding shallow structures.

According to Equation (6), the depth to the basement surface was calculated by dividing the values of the AS map (Fig. 15) by those of the AS1 map (Fig. 16) and multiplying by a scaling factor of 1. The resulting analytical signal depth map (Fig. 17) shows depth values ranging from -6 meters to -78 meters across the study area.

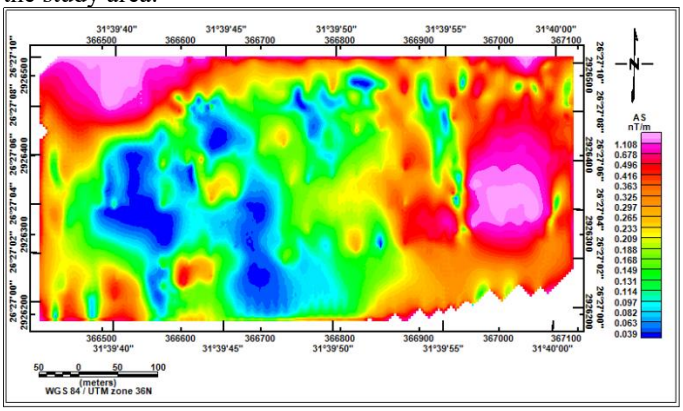

Figure 15: Analytical signal (AS) map of the studied area.

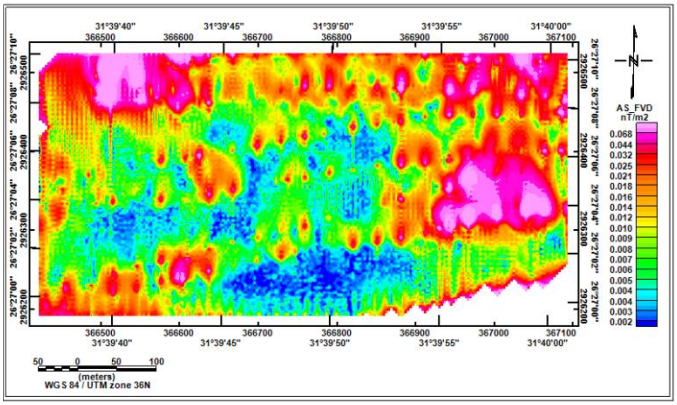

Figure 16: Analytical signal of the first vertical drevative (AS_FVD) map of the studied area.

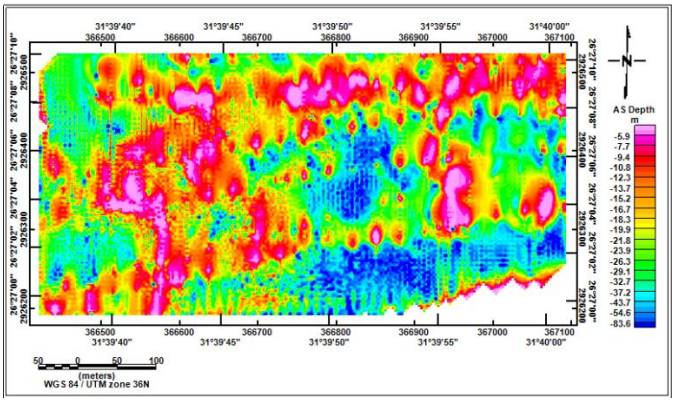

Figure 17: Analytical signal depth (AS_Depth) map of the studied area.

5.5.2. The source parameter imaging (SPI) map

The Source Parameter Imaging (SPI) map (Fig. 18) provides an estimation of the depth to magnetic sources within the study area. The SPI technique is an automated method that calculates source depths based on the local gradients of the magnetic field. The depth values obtained from the SPI map range between -8 meters and -75 meters, showing good agreement with the depth estimates derived from the analytical signal (AS) depth map (Fig. 17).

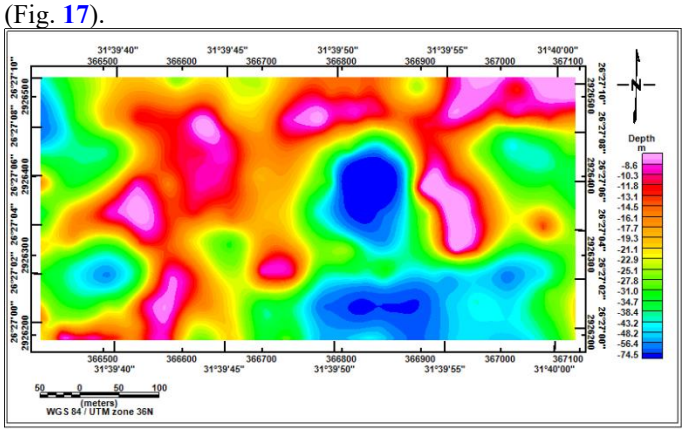

Figure 18: Source parameter imaging (SPI) map of the studied area.

5.5.3. The Euler deconvolution (ED) map

The 3D Euler Deconvolution technique was applied to the gridded magnetic data using Geosoft Oasis Montaj software, version 8.4, [14] to identify subsurface structural features, particularly geological contacts and fault zones. In this analysis, two structural indices (SI) were selected to target different types of magnetic sources.

For detecting simple geological contacts (such as lithological boundaries or abrupt changes in susceptibility), an SI value of 0 was used. The analysis employed a window size of 10 × 10 grid cells, with each cell measuring 30.5 meters, and a maximum depth tolerance of 15% to ensure consistent depth estimates.

To identify vertical or dipping geological features including faults, fractures, dykes, and steeply dipping bodies an SI value of 1 was selected. In this case, a larger window size of 20 × 20 grid cell size was used, with each cell measuring 61 meters, while maintaining the same 15% maximum depth tolerance to control for depth estimation accuracy.

The resulting Euler solution map with SI = 0 (Fig. 19) illustrates subsurface structures with depth estimates ranging from less than 20 meters to over 60 meters, with an average depth of approximately 16.5 meters. This map effectively outlines contact zones within the study area.

Similarly, the Euler solution map with SI = 1 (Fig. 20) reveals structural features at depths ranging from less than 20 meters to over 60 meters, with an average depth of around 32 meters. This map emphasizes deeper-seated structural features such as faults, fractures, dykes, and steep lithological contacts, which tend to have more complex geometries and magnetic signatures than simple near-surface contacts.

Both maps show well-defined clusters of solution points that align in linear and curvilinear patterns. These alignments reflect the structural fabric of the study area and suggest potential interactions between different rock units, offering valuable insights into the subsurface geological framework.

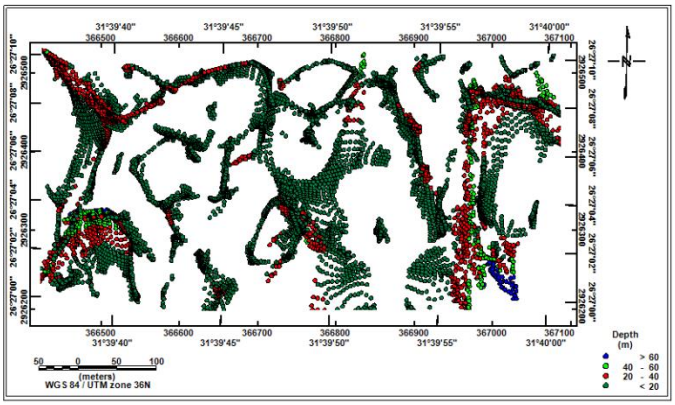

Figure 19: Euler deconvolution (ED) map with SI = 0 of the studied area.

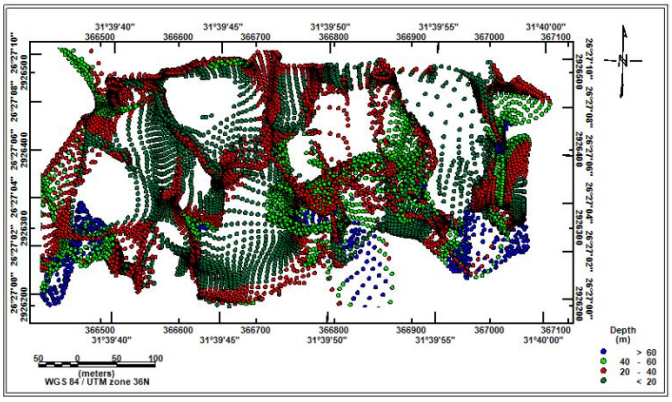

Figure 20: Euler deconvolution (ED) map with SI = 1 of the studied area.

5.6. Structural lineaments of magnetic data.

The Center for Exploration Targeting (CET) Grid Analysis extension in Oasis Montaj™ was utilized to analyze the RTP, regional, and residual magnetic data of the study area. This extension provides a comprehensive set of tools for the automated extraction of structural lineaments from gridded datasets.

5.6.1. RTP map analysis

The structural lineaments identified from the RTP magnetic map are presented in Figure 21a, where they are overlaid on the RTP map itself. Figure 21b displays the rose diagram generated from the orientation analysis of these lineaments, illustrating their azimuthal distribution and highlighting the dominant structural trends based on their orientation and frequency. The analysis reveals a prevailing trend in the near (N-S) direction.

A detailed statistical summary of the extracted lineaments from the RTP map is provided in Table 2. The table classifies the lineaments by azimuthal ranges, presenting the number of lineaments (N), total length of lineaments (L, in meters), the percentage of total lineaments (N%), the percentage of total lineament length (L%), and the average length per lineament (L/N) for each directional interval.

The results indicate that the most dominant structural trend falls within the 0° to <10° azimuth range (near N-S direction), comprising 46 lineaments (24% of total) with a combined length of 935 meters (28% of total length). Another significant trend appears in the east-west (E-W) direction, within the 90° to <100° azimuth range, containing 27 lineaments (14% of total) with a total length of 386 meters (11% of total length).

In total, 194 lineaments were identified (ΣN), with a cumulative length of 3393 meters (ΣL). Both ΣN% and ΣL% were normalized to 100%.

5.6.2. Regional map analysis

Similarly, CET was applied to the regional magnetic map to get deep lineaments. The extracted lineaments are displayed in Figure 22a, with the corresponding rose diagram shown in Figure 22b. Statistical results are summarized in Table 3.

This analysis also revealed a dominant N-S trend, specifically in the 0° to <10° azimuth range, with 24 lineaments (20% of total) totaling 584 meters (18% of total length). Additionally, a prominent E-W trend was observed in the 90° to <100° azimuth range, comprising 21 lineaments (18% of total) with a cumulative length of 900 meters (28% of total length).

The red mean arrow shows the average orientation of all the structural measurements which is the dominant trend in the Nile Valley area.

The total number of extracted lineaments from the regional map is 120 (ΣN), with an overall length of 3259 meters (ΣL), with normalized percentages.

3. Residual Map Analysis

Finally, CET was applied to the residual magnetic map, which highlights the shallowest structures. The detected lineaments are illustrated in Figure 23a, with their orientation distribution shown in the rose diagram in Figure 23b. Table 4 provides the corresponding statistical summary.

The analysis indicates a dominant N-S trend (0° to <10° azimuth range), consisting of 56 lineaments (27% of total) with a total length of 1003 meters (28% of total length). The E-W trend (90° to <100° azimuth range) also stands out, containing 28 lineaments (14% of total) with a cumulative length of 480 meters (13% of total length).

In total, 209 lineaments were identified (ΣN) from the residual map, with a combined length of 3559 meters (ΣL), with normalized percentages.

The identified structural trends in the study area, including N–S, E–W, and NW–SE orientations, are consistent with the principal tectonic directions observed across Egypt. The N–S trend aligns with the structural framework of the Nile Valley and the Red Sea rift system, reflecting extensional and strike-slip movements active since the Neogene. The E–W trend corresponds to the Tethyan structural grain, inherited from the Mesozoic closure of the Neo-Tethys Ocean and preserved in the basement fabric. The NW–SE structures are associated with the Gulf of Suez rift trend, which has been active since the Oligocene. The structure lineaments that deduced are coinside with the results of Elbadrawy et al. [46], Beshr et al., [47] and Ibraheem et al. [48].

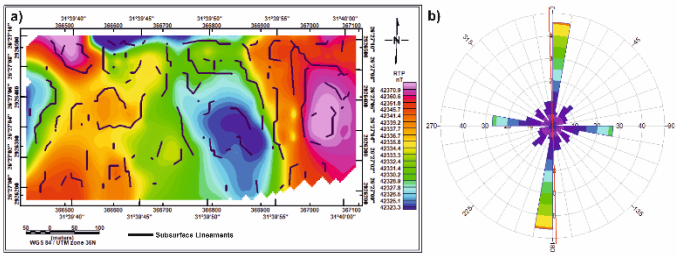

Figure 21: a) The structure lineaments extracted from and plotted on RTP map of the studied area b) Frequency bearing rose diagram deduced from lineaments extracted from RTP map.

Table 2: Statical analysis of lineaments bearing from RTP map.

No.	Azimuth	N	L	N%	L%	L/N
1	0° - < 10°	46	935	24	28	20
2	10° - < 20°	6	96	3	3	16
3	20° - < 30°	4	41	2	1	10
4	30° - < 40°	10	163	5	5	16
5	40° - < 50°	12	134	6	4	11
6	50° - < 60°	7	97	4	3	14
7	60° - < 70°	7	88	4	3	13
8	70° - < 80°	6	85	3	3	14
9	80° - < 90°	1	19	1	1	19
10	90° - < 100°	27	386	14	11	14
11	100° - < 110°	12	195	6	6	16
12	110° - < 120°	4	55	2	2	14
13	120° - < 130°	9	119	5	4	13
14	130° - < 140°	10	143	5	4	14
15	140° - < 150°	3	48	2	1	16
16	150° - < 160°	8	201	4	6	25
17	160° - < 170°	11	201	6	6	18
18	170° - < 180°	11	387	6	11	35
Total		194	3393	100	100	

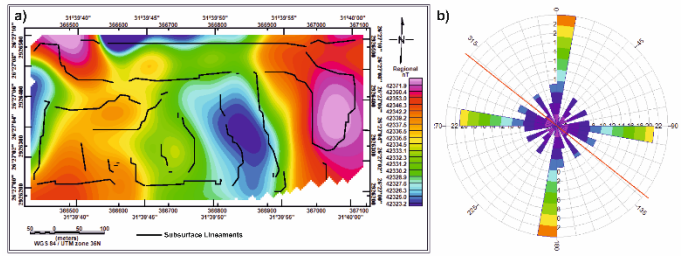

Figure 22: a) The structure lineaments extracted from and plotted on regional magnetic map of the studied area b) Frequency bearing rose diagram deduced from lineaments extracted from regional magnetic map.

Table 3: Statical analysis of lineaments bearing from regional map.

No.	Azimuth	N	L	N%	L%	L/N
1	0° - < 10°	24	584	20	18	24
2	10° - < 20°	2	35	2	1	18
3	20° - < 30°	1	14	1	0	14
4	30° - < 40°	7	129	6	4	18
5	40° - < 50°	4	61	3	2	15
6	50° - < 60°	2	39	2	1	20
7	60° - < 70°	7	81	6	2	12
8	70° - < 80°	1	13	1	0	13
9	80° - < 90°	7	447	6	14	64
10	90° - < 100°	21	900	18	28	43
11	100° - < 110°	7	150	6	5	21
12	110° - < 120°	9	145	8	4	16
13	120° - < 130°	3	51	3	2	17
14	130° - < 140°	3	26	3	1	9
15	140° - < 150°	8	176	7	5	22
16	150° - < 160°	0	0	0	0	-
17	160° - < 170°	5	95	4	3	19
18	170° - < 180°	9	313	8	10	35
Total		120	3259	100	100	

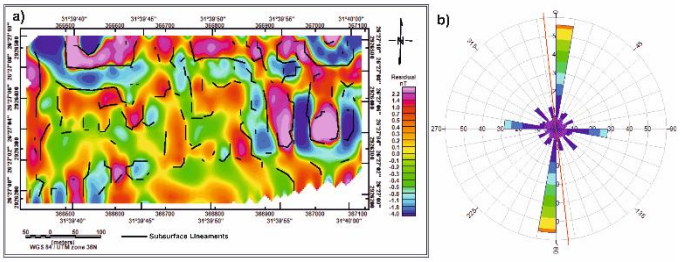

Figure 23: a) The structure lineaments extracted from and plotted on residual magnetic map of the studied area b) Frequency bearing rose diagram deduced from lineaments extracted from residual magnetic map.

Table 4: Statical analysis of lineaments bearing from residual map.

No.	Azimuth	N	L	N%	L%	L/N
1	0° - < 10°	56	1003	27	28	18
2	10° - < 20°	5	80	2	2	16
3	20° - < 30°	9	133	4	4	15
4	30° - < 40°	10	178	5	5	18
5	40° - < 50°	5	48	2	1	10
6	50° - < 60°	4	53	2	1	13
7	60° - < 70°	10	136	5	4	14
8	70° - < 80°	6	89	3	3	15
9	80° - < 90°	5	133	2	4	27
10	90° - < 100°	28	480	14	13	17
11	100° - < 110°	9	135	4	4	15
12	110° - < 120°	8	100	4	3	13
13	120° - < 130°	6	97	3	3	16
14	130° - < 140°	15	205	7	6	14
15	140° - < 150°	5	75	2	2	15
16	150° - < 160°	5	74	2	2	15
17	160° - < 170°	12	233	6	7	19
18	170° - < 180°	7	307	3	9	44
Total		205	3559	100	100	

6. Conclusion

This investigation highlights the successful application of ground magnetic surveying for the identification of shallow subsurface structural lineaments within the Sohag University campus at El-Kawamel. The survey covered approximately 0.2 square kilometers, employing a high-sensitivity GEM GSM-19 Overhauser magnetometer. Six east-west oriented profiles were systematically distributed across the site at 50-meter intervals, following a zigzag acquisition pattern. A total of 1487 magnetic readings were collected, ensuring high-density coverage and consistent data quality. Through advanced filtering and depth estimation techniques using Geosoft Oesis Montaj ver 8.4, the survey effectively delineated both shallow and deep magnetic sources, with depths ranging from approximately 6 meters to over 75 meters. The magnetic data revealed major structural trends oriented predominantly in the N-S, E-W and NW-SE directions, aligning well with the region's dominant tectonic trends. These structures, including faults, fractures, and boundaries, are critical considerations for future engineering projects in the area.

Edge detection methods (TDR, THDR_TDR, FVD, HG, and SED) provided detailed mapping of fault zones and subsurface contacts, while depth estimation methods such as analytic signal, SPI, and Euler deconvolution yielded consistent and reliable depth values. The lineament analysis revealed significant clustering of structural features, indicating zones of structural weakness that may affect future construction activities.

Overall, this study confirms the capability of the ground magnetic method as an efficient, non-invasive tool for subsurface site investigations in engineering applications. The integrated approach combining detailed magnetic surveying, geological knowledge, and advanced processing techniques presents a comprehensive framework for assessing potential geohazards in construction sites.

It's recommended for the future work that the area will involve integrating magnetic data with Very Low Frequency (VLF), seismic methods, and electrical resistivity tomography (ERT) along with 3D geophysical modeling to enhance subsurface imaging for engineering planning.

CrediT authorship contribution statement:

Author Contributions: For research articles with several authors, a short paragraph specifying their individual contributions must be provided. The following statements should be used "Conceptualization, Abudeif, A.M., Mohammed, M.A., Khalifa, M.M., Gaber, H.A.,; methodology, Abudeif, A.M., Mohammed, M.A., Gaber, H.A.,: software, Abudeif, A.M., Mohammed, M.A., Khalifa, M.M., Gaber, H.A., Mahmoud, M.I.,; validation, Abudeif, A.M., Mohammed, M.A., Attia, M.M.,; formal analysis, Abudeif, A.M., Mohammed, M.A., Attia, M.M., Gaber, H.A.,; investigation, Abudeif, A.M., Mohammed, M.A., Khalifa, M.M., Gaber, H.A., Mahmoud, M.I.,; resources, Abudeif, A.M., Mohammed, M.A., Attia, M.M., Mahmoud, M.I.,; data curation, Abudeif, A.M., Mohammed, M.A., Gaber, H.A.,; writing—original draft preparation, Abudeif, A.M., Mohammed, M.A., Gaber, H.A., Mahmoud, M.I.,; writing—review and editing, Abudeif, A.M., Mohammed, M.A., Gaber, H.A.,; visualization, Abudeif, A.M., Mohammed, M.A., Attia, M.M., Khalifa, M.M.,; supervision, Abudeif, A.M., Mohammed, M.A., Attia, M.M.,; project administration, No.; funding acquisition, No. All authors have read and agreed to the published version of the manuscript."

Data availability statement

The data used to support the findings of this study are available from the corresponding author upon request.

Declaration of competing interest

The authors declare that they have no known competing financial interests or personal relationships that could have appeared to influence the work reported in this paper.

Acknowledgments

The authors express their sincere gratitude to the Geology Department, Faculty of Science, Sohag University, for their support and provision of equipment used during data acquisition.

References

[1] G.E. Omolaiye, A.K. Oniyangi, T.A. Issa and S.B. Adam, *Discover Geoscience*, 2(1), (2024) pp.1-25.

[2] L.A. Olayinka, K.M. Lawal, A.L. Ahmed, B.G. Aremu, F. Abubakar, A. Usman and E. Daniel, *Applied Journal of Physical Science,* 1(2), (2019) pp.14-23.

[3] A.K. Abd El Aal, B.S. Nabawy, A. Aqeel, and A. Abidi, *Journal of African Earth Sciences,* 161, (2020) p.103671.

[4] P.M. Soupios, P. Georgakopoulos, N. Papadopoulos, V. Saltas, A. Andreadakis, F. Vallianatos, A. Sarris and J.P., Makris, *Journal of Geophysics and Engineering*, *4*(1), (2007) pp.94-103.

[5] T. Mahran, *Arabian Journal of Geosciences*, 17(9), (2024) p.250.
[6] H. A. Mostafa, Geological Studies on the Area Northeast of Sohag. M. Sc. Thesis, Geology Department, Faculty of Science, Assiut University: Assiut, Egypt, 259p. 1979.
[7] B. El-Haddad, *Evolution of the geological history of the Egyptian Nile at Sohag area using sedimentological studies and remote sensing techniques.* Sc Geology dept., Faculty of Science, Sohag Univ, 2014.
[8] R. Said, The geological evolution of the River Nile. Springer New York, NY, 1981.
[9] A. Omer, Geological, mineralogical and geochemical studies on the Neogene and Quaternary Nile basin deposits, Qena-Assiutstretch, Egypt. Ph.D. Thesis, South Valley University, Sohag, Egypt, 320 p. 1996.
[10] S. Ahmed, *Geology of the area east and southeast of Sohag.* Master's Thesis, Geology Department, Faculty of Science, Assiut University, Assiut, Egypt, 1980.
[11] T. Mahran, and A.M. Hassan, *Journal of African Earth Sciences,* 199, (2023) p.104829.
[12] T. Mahran, A. El Haddad, *Journal of Saharian Studies.* 1, (1992) pp.11–40.
[13] M.I. Youssef, *AAPG Bull,* 52, (1968**)** pp.601–614.
[14] Y. Li, and D.W. Oldenburg, *Geophysics*, *63*(2), (1998) pp.431-439.
[15] R.J. Blakely, *Cambridge university press*, (1996)
[16] A. Spector and F.S. Grant, *Geophysics,* 35(2),(1970) pp.293-302.
[17] H.G. Miller and V. Singh, *Journal of applied Geophysics*, 32(2-3), (1994) pp.213-217.
[18] B. Verduzco, J.D. Fairhead, C.M. Green, and C. MacKenzie, *The leading edge*, 23(2), (2004) pp.116-119.
[19] Geosoft oasis montaj, V.8.4: Geosoft Software for the Earth Science, Geosoft Inc., *Toronto, Canada* (2015).
[20] A. Salem, S. Williams, D. Fairhead, R. Smith and D. Ravat, *Geophysics*, 73(1),(2008) pp.L1-L10.
[21] A. Salem, S. Williams, J.D. Fairhead, D. Ravat and R. Smith, *The leading edge*, *26*(12), (2007) pp.1502-1505.
[22] W.J. Hinze, R.R. Von Frese, R. Von Frese, and A.H. Saad, Gravity and magnetic exploration: Principles, practices, and applications. Cambridge University Press.*Cambridge University Press*, 2013.
[23] P. Hood, and D.J., McClure, *Geophysics,* 30(3), (1965) pp.403-410.
[24] W.R., Roest, J.J., Dañobeitia, J.Verhoef, and B.J. Collette, *Marine Geophysical Researches*, *14*,(1992) pp.1-24.
[25] G.M. Gaber, S. Saleh, and M. Toni, *Acta Geophysica*, 70(2), (2022) pp.639-657.
[26] W. Araby, S.H. Abd, A.E. Aref, I. Al-Alfy, M.M. Abdullah and A.A., Elhusseiny, *The Leading Edge,* 40(10), (2021) pp.724-733.
[27] J.D. Phillips, *SEG Technical Program Expanded Abstracts* (2000) pp. 402-405.
[28] N. Whitehead, and C. Musselman, *Oasis MontajTM: Tutorial and User Guide.* (2005) Version, 6.
[29] A.M. Eldosouky, and S.A. Saada, *Arabian Journal of Geosciences,* 13,(2020) pp.1-12.
[30] M.N. Nabighian, *Geophysics*, 37(3),(1972) pp.507-517.
[31] I.N. MacLeod, K. Jones and T.F. Dai, *Exploration geophysics*, *24*(4),(1993) pp.679-688.
[32] A.B. Reid, J.M. Allsop, H. Granser, A.T. Millett and I.W. Somerton, *Geophysics*, *55*(1),(1990) pp.80-91.
[33] J.B. Thurston and R.S. Smith, *Geophysics, 62*(3), (1997) pp.807-813.
[34] R.S. Smith, J.B. Thurston, T.F. Dai and I.N. MacLeod, *Geophysical prospecting*, 46(2), (1998) pp.141-151.
[35] D.T. Thompson, *Geophysics*, 47(1), (1982) pp.31-37.
[36] M. Fedi, *Fractal solutions for understanding complex systems in Earth sciences* (2015) pp. 1-18.
[37] A.B. Reid, and J.B. Thurston, *Geophysics*, *79*(4), (2014). pp.J61-J66.
[38] V.C. Barbosa, J.B. Silva and W.E. Medeiros, *Geophysics*, *64*(1), (1999). pp.48-60.
[39] A. Salem, and D. Ravat, *Geophysics*, *68*(6), (2003) pp.1952-1961.
[40] F.F. Melo, and V.C. Barbosa, *Geophysics*, 83(6), (2018) pp.J87-J98.
[41] Rockware, *Rockworks software package, Rockworks 16 user manual*. Rockware Incorporated. (2011).
[42] A.M. Abudeif, M.A Ali,. and M.A. Mohammed, *Sohag Journal of Sciences*, *8*(3), (2023) pp.337-346.
[43] M. El Bohoty, A. Khalil, W. Hassan, A. El-Kotb, A. Awad and M. Khalifa, *NRIAG Journal of Astronomy and Geophysics*, 10(1), (2021) pp.218-234.
[44] M. Rajaram, *Geohorizons, 50, (*2009) *p*.
[45] A.M. Abudeif, M.M. Senosy, F.A. Mahmoud and M.A. Shelkamy, *Sohag Journal of Sciences*, 10(1), (2025) pp.103-115.
[46] H.T. El-Badrawy, A.M. Abbas, U. Massoud, T. Abu-Alam, H.A. Alrefaee, S.M. Abo Khashaba, and M. Nagy,. *Frontiers in Earth Science*, 12, (2024) p.1456055.
[47] A.M. Beshr, A.K. Mohamed, A. ElGalladi, , A. Gaber, and F. El-Baz, *The Egyptian Journal of Remote Sensing and Space Science,* 24(3), (2021) pp.999-1011.
[48] I.M. Ibraheem, M. Haggag, and B. Tezkan,. *Geosciences*, 9(5), (2019) p.211.